Lasing in Si$_3$N$_4$-organic hybrid (SiNOH) waveguides

DARIA KOHLER,[1,2] ISABEL ALLEGRO,[2] SENTAYEHU FETENE WONDIMU,[1,2] LOTHAR HAHN,[2] WOLFGANG FREUDE,[1] 🆔 AND CHRISTIAN KOOS[1,2,*] 🆔

[1]*Institute of Photonics and Quantum Electronics (IPQ), Karlsruhe Institute of Technology (KIT), Engesserstrasse 5, 76131 Karlsruhe, Germany*
[2]*Institute of Microstructure Technology (IMT), Karlsruhe Institute of Technology (KIT), Hermann-von-Helmholtz-Platz 1, 76344 Eggenstein-Leopoldshafen, Germany*
[*]*christian.koos@kit.edu*

Abstract: Silicon nitride (Si$_3$N$_4$) waveguides offer low-loss wave propagation over a wide spectral range including visible wavelengths and lend themselves to photonic integrated circuits for bio-photonic applications. The Si$_3$N$_4$ device portfolio, however, is so far limited to passive devices that need to be fed by external light sources. This often requires delicate and costly fiber-chip coupling schemes that are subject to stringent alignment tolerances. In this paper, we present and investigate a class of lasers that combine Si$_3$N$_4$ waveguides with light-emitting organic cladding materials in a hybrid approach. These Si$_3$N$_4$-organic hybrid (SiNOH) lasers are operated by optical pumping from the top with low alignment precision. We theoretically and experimentally investigate different SiNOH laser concepts based on spiral-shaped ring resonators and distributed feedback (DFB) resonators. While our devices are designed for an emission wavelength of approximately 600 nm, the SiNOH laser concept can be transferred to a large range of wavelengths in the visible spectrum. The devices are amenable to cost-efficient mass production and have the potential to address a wide range of applications in bio-photonics and point-of-care diagnostics.

1. Introduction

Integrated sensors based on optical waveguides (WG) have an enormous potential in bio-photonics and in biomedical diagnostics, especially when it comes to multiplexed and highly sensitive detection of a wide variety of target molecules [1,2]. For bio-photonic applications, operation in the visible wavelength range is particularly interesting due to the low absorption in aqueous solutions, which allows for large interaction lengths in refractive-index sensors [3], enables low-background absorption spectroscopy with large dynamic range [4], or is instrumental to living-cell imaging via WG-based total internal reflection fluorescence (TIRF) microscopy [5]. Specifically, absorption in typical aqueous analytes, such as urine or saliva, is approximately three orders of magnitude smaller at visible (VIS) wavelengths of, e.g., 600 nm than at near-infrared (NIR) wavelengths of, e.g., 1550 nm [6]. Similarly, blood analysis in photonic sensors largely relies on the so-called therapeutic window between 600 nm and 1100 nm which offers a good compromise between pronounced hemoglobin absorption at shorter wavelengths and strong water absorption at longer wavelengths [7].

In this context, silicon nitride (Si$_3$N$_4$) has emerged as a highly attractive integration platform for WG-based sensors, offering low-loss propagation over a wide spectral range from VIS to NIR wavelengths [8–11]. Silicon nitride WG feature a high refractive-index contrast between the core ($n_{Si_3N_4} = 2.02$ @ $\lambda = 600$ nm [12]) and the silicon dioxide cladding ($n_{SiO_2} = 1.46$ @ $\lambda = 600$ nm [13]) or the aqueous analyte ($n_{H_2O} = 1.33$ @ $\lambda = 600$ nm [14]) and are therefore perfectly suited for densely integrated sensor arrays with small footprint and low analyte consumption. Moreover,

Si_3N_4-based photonic integrated circuits (PIC) can be efficiently fabricated in large quantities using mature wafer-scale processes that exploit the CMOS technology base and that are accessible through a world-wide ecosystem of photonic foundries [8,9,11]. This opens a path towards cost-efficient mass production of highly functional sensor chips for one-time use in point-of-care diagnostics.

However, despite its various advantages, the basic Si_3N_4 integration platform is so far limited to passive building blocks. Silicon nitride PIC hence have to rely either on external light sources that are coupled to the optical sensor chip [3,15,16], or on a hybrid integration of light-emitting materials in combination with passive Si_3N_4 WG [17–19]. Light supplied by external sources requires delicate fiber-chip coupling schemes that are subject to stringent mechanical tolerances, and the associated complexity is prohibitive for low-cost disposable sensors. Moreover, grating couplers, which are the mainstay for fiber-chip coupling in silicon photonics, suffer from low refractive-index contrast when realized on the Si_3N_4 platform. This leads to low grating strength, poor directionality, and low coupling efficiencies [20]. These challenges can be overcome by on-chip light sources. Previous demonstrations of visible-light sources on the Si_3N_4 platform comprise DFB resonators with CdS/CdSe quantum dots [21] as the gain material. Further investigations concentrated on ring and disk resonators that are vertically coupled to Si_3N_4 WG cores and that contain perovskites [22,23] or CdS/CdSe quantum dots [24] light-as emitting material. However, these approaches require comparatively complex manufacturing processes, including material deposition from the gas phase and subsequent lithographic structuring. For disposable point-of-care sensors, highly scalable low-cost fabrication techniques for light sources would be advantageous.

In this paper we expand on our previous demonstrations [25] of a new class of laser sources that can be efficiently integrated on the Si_3N_4 platform using low-cost fabrication techniques without any additional lithographic structuring. The devices rely on a hybrid approach that combines nanophotonic Si_3N_4 WG cores with dye-doped organic cladding materials which can be optically pumped by an external laser or a light-emitting diode (LED) without any high-precision alignment of the pump spot and without any mechanical contact to the chip. The dye-doped organic cladding can be efficiently deposited on the wafer by spin coating, by local dispensing, or by inkjet printing. An appropriate choice of laser dyes and cavity designs would allow to integrate a multitude Si_3N_4-organic hybrid (SiNOH) lasers with various emission wavelengths across the VIS and NIR spectral ranges on a common substrate. In our work, we develop a theoretical model of SiNOH lasers for spiral-shaped ring resonators and for distributed-feedback (DFB) resonators, and we experimentally demonstrate lasing in both structure types. In combination with simple camera read-out schemes, our concept shows a route towards disposable sensor chips for highly multiplexed detection of a wide range of analytes in point-of-care diagnostics. During the preparation of this manuscript, the concept of SiNOH lasers [25,26] was independently demonstrated by another group [27,28] using second-order DFB structures that are amenable to production with relaxed lithography resolution requirements. These experiments prove the viability of the concept and demonstrate its transferability to different photonic integration platforms.

2. Si_3N_4-organic hybrid device concept and design considerations

The basic concept of Si_3N_4-organic hybrid (SiNOH) lasers [25] is illustrated in Fig. 1. The SiNOH lasers are optically pumped from the top by an external light source, see Fig. 1(a). High-precision alignment of the pump spot is not required, and the scheme lends itself to integration of laser arrays with individually defined emission wavelengths $\lambda_{1...n}$. The SiNOH laser light is emitted directly into Si_3N_4 single-mode WG and can be efficiently coupled to a subsequent sensor array, here illustrated as Mach-Zehnder interferometers. At the sensor outputs, light is radiated into free space via grating couplers and captured by a camera. This concept allows for contact-less
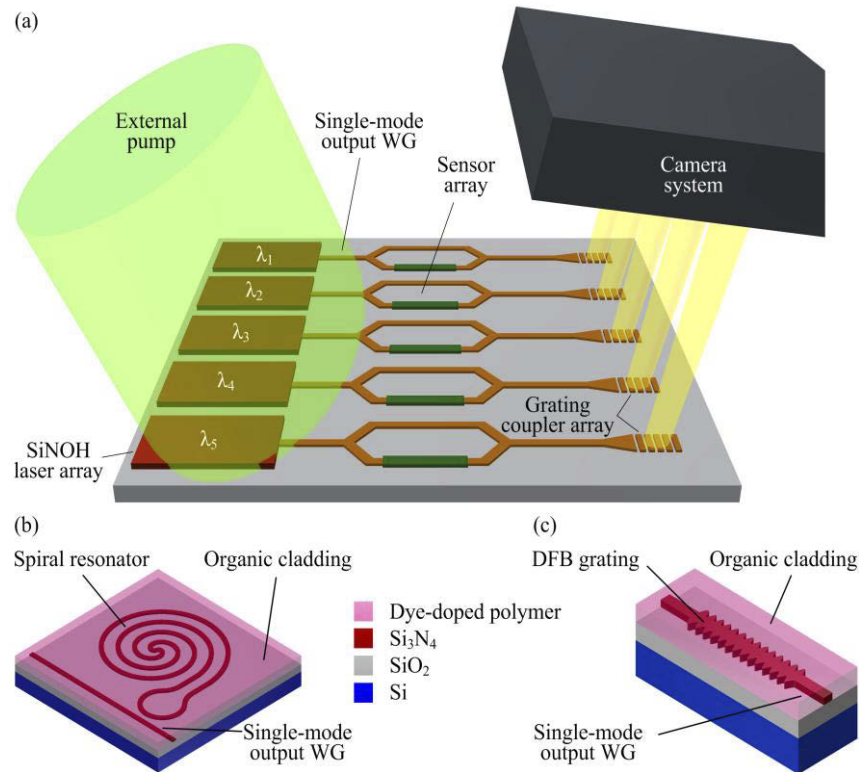
Fig. 1. Basic concept of integrated Si_3N_4-organic hybrid (SiNOH) lasers. (a) SiNOH lasers feeding an array of waveguide-based sensors. The lasers are optically pumped from the top by an external light source illuminating an extended spot, without any need for high-precision mechanical alignment. Laser light is emitted directly into the Si_3N_4 single-mode WG and can hence be efficiently coupled to an array of on-chip sensors, here illustrated as Mach-Zehnder interferometers. The light from the sensor output is radiated to the top by grating couplers and captured by a camera. (b) SiNOH laser with spiral-shaped resonator. The active WG consists of a Si_3N_4 core with a dye-doped organic cladding as a gain medium. An appropriate resonator design in combination with a suitable gain medium allows to realize various emission wavelengths $\lambda_{1...n}$ on the same chip. The ring resonator is coiled up into a double spiral and coupled evanescently to a single-mode output WG. (c) SiNOH laser with distributed-feedback (DFB) resonator, formed by a strip WG with periodic sidewall corrugations.

excitation and readout of large-scale sensor arrays on technically simple low-cost optical sensor chips.

2.1. Device concept

The active SiNOH WG have a Si_3N_4 core on top of a silicon dioxide bottom cladding, see Figs. 1(b) and 1(c). Optical gain is provided by an organic top cladding that is doped with a light-emitting dye. By appropriate choice of the gain medium and of the device design, various emission wavelengths $\lambda_{1\ldots n}$ can be realized on the same chip. These devices can be pumped with a single light source such as an LED. SiNOH lasers of different wavelengths can be realized by either choosing individual gain materials or by combining a single broadband gain material with different resonator designs. On the silicon platform, we have previously demonstrated similar concepts for on-chip lasers emitting in the NIR [29].

In our experiments, we investigate two laser resonator types: A spiral-shaped ring resonator, Fig. 1(b), and a distributed-feedback (DFB) structure, Fig. 1(c). The ring resonator is coiled up into a long double spiral and is coupled evanescently to a single-mode output WG, Fig. 1(b). Compared to the DFB laser, the double spiral covers a much larger chip area and hence offers a better overlap with a moderately focused pump beam that leads to relaxed alignment tolerances. The DFB resonator is formed by a straight strip WG with sidewall corrugations, Fig. 1(c). The footprint of the DFB resonator is small such that many SiNOH lasers can be pumped simultaneously with one pump beam. The DFB structure supports lasing in basically two longitudinal modes spectrally located at both edges of the Bragg stop-band. Asymmetries or a quarter-wavelength defect reduce the number of lasing modes to one. Pump efficiency, threshold and spectral properties depend strongly on the modal gain and on the loss of the respective laser types - this is discussed in more detail in the following subsections. For the devices shown in this work, we use first-order Bragg gratings with a period of approximately 170 nm, which requires comparatively high lithography resolution. It has recently been demonstrated that SiNOH DFB lasers can also be realized with second-order gratings [27,28], having grating periods of more than 350 nm. Such structures are amenable to high-throughput mass fabrication using, e.g., 248 nm deep-UV lithography.

2.2. Gain and loss in SiNOH WG

The power of the oscillating laser mode depends on the SiNOH WG loss and on the efficiency with which the pump is coupled to the active WG region. Within the resonator, the waves experience a net power gain of $G = \exp[(g - \alpha)2L]$ for one round-trip of length $2L$, where g and α denote the effective modal power gain and loss coefficients (unit cm^{-1}) of the laser cavity. In the case of a ring resonator, $2L$ denotes the ring perimeter, while for the case of a DFB laser L represents the geometrical resonator length.

The gain of the laser resonator results from the interaction of the evanescent parts of the WG mode with the dye molecules in the organic top cladding, which are optically excited by the pump light. The simulated electric field magnitudes $|\vec{E}|$ of the quasi-TE and quasi-TM modes in the cross-section of a strip WG are shown in Figs. 2(a) and 2(b), respectively. Figures 2(d)–2(e) display the field distribution of a DFB mode at the upper and the lower edge of the stop-band. Note that the terms "upper" and "lower" refer to optical frequency or photon energy and not to wavelength.

Gain and loss in ring resonators For ring resonators, the optical loss of the laser cavity is caused by attenuation of the mode when propagating along the ring, and by the power output coupling $|\kappa_r|^2$ to the bus WG [30]. The net round-trip power gain and the net modal gain at threshold is therefore

$$G = e^{(g_{th}-\alpha)2L}(1 - |\kappa_r|^2) = 1, \qquad (g_{th} - \alpha)2L = -\ln(1 - |\kappa_r|^2). \tag{1}$$
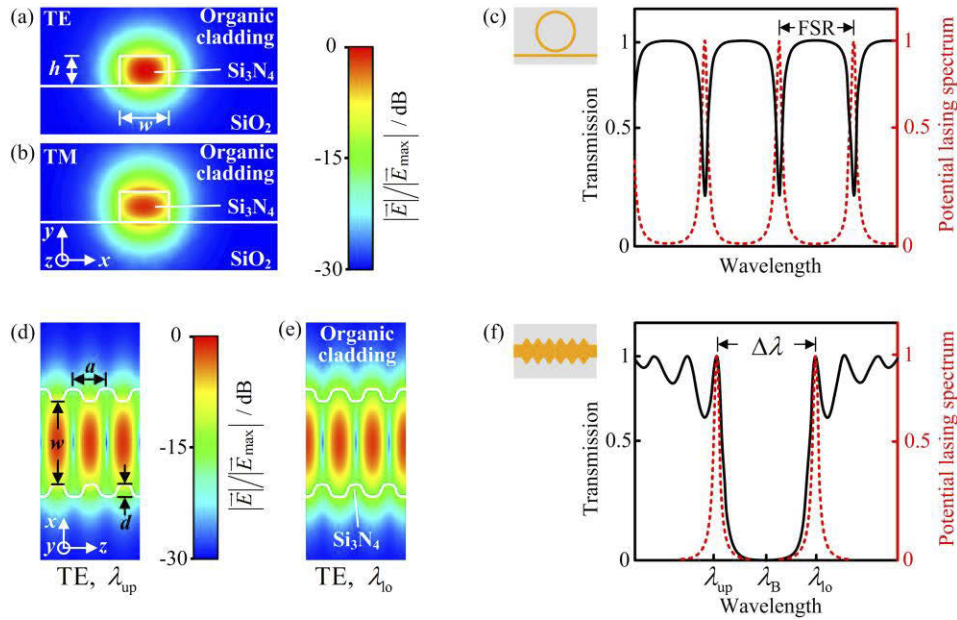
Fig. 2. Waveguide (WG) and resonator concepts of SiNOH lasers. (a),(b) Strip WG used for ring-resonator SiNOH lasers: The graph shows the WG cross section (width w, height h) along with the simulated electric field magnitudes $|\vec{E}|$ of the fundamental quasi-TE mode (a) and the fundamental quasi-TM mode (b). (c) Ring-resonator cavity: Schematic power transmission between the input and the output of the straight bus WG (black solid line) as a function of the vacuum wavelength λ. Lasing occurs at the resonances (red dashed line) marked by notches in the transmission. For the devices used in this publication, the ring-resonator WG are coiled up to form spirals, see Fig. 1(b). (d),(e) Distributed-feedback (DFB) structures: Top view of corrugated strip WG (width w, height h, corrugation period a, and corrugation depth d), along with the simulated electric field magnitudes $|\vec{E}|$ of the DFB mode at the upper band edge with larger photon energy and short-wavelength resonance λ_{up} (d) as well as at the lower band edge with smaller photon energy and long-wavelength resonance λ_{lo} (e). All mode fields are plotted in the plane $y = h/2$. (f) DFB resonator: Schematic power transmission between the input and the output of the corrugated section (black solid line) as a function of the vacuum wavelength λ. For a DFB grating without phase shift, lasing occurs at the upper or lower edge of the stop-band (red dashed lines).

Gain and loss in DFB resonators For DFB lasers, the resonator mode can be described by two counter-propagating waves. The grating couples these waves with a coupling factor κ. In the following, we assume the coupling factor to be real-valued, $\kappa \in \mathbb{R}$, i.e., the propagating mode only experiences a periodic perturbation of the refractive index, but not of the modal gain [31]. This assumption is based on the observation that the periodic sidewall corrugation does not affect the penetration depth of the evanescent field into the cladding to a substantial degree. For low gain, $\frac{1}{2}(g - \alpha) \ll \kappa$, the first-order resonances of a DFB laser are at the stop-band edges, and the net modal threshold power gain g_{th} can be approximated by [31, Eqs. (29) and (6)]

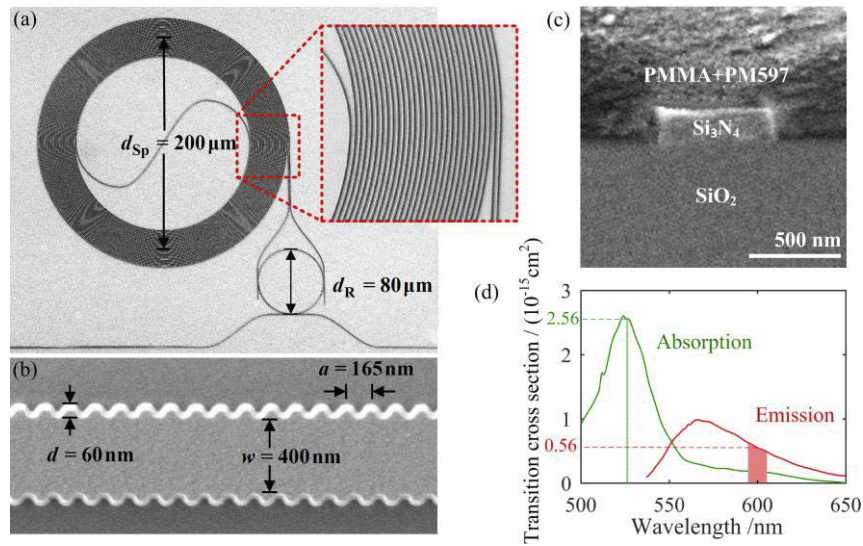$$(g_{\mathrm{th}} - \alpha)L = 2\left(\frac{\pi}{\kappa L}\right)^2. \tag{2}$$

Fig. 3. SEM images of the Si_3N_4 WG with spectra of the absorption and emission cross sections of the organic dye, dispersed in the PMMA cladding. (a) Spiral resonator: To improve the overlap with the pump, the ring resonator WG is coiled up densely to form a double spiral with a minimal curvature radius of 40 µm in the center. (b) DFB resonator: Corrugated WG with width w, corrugation depth d, and period a. (c) Cross-section of the Si_3N_4 WG core clad with PMMA and Pyrromethene (PM597). (d) Emission and absorption cross-sections of PM597 embedded in a PMMA matrix. The material is pumped by a laser, emitting near the absorption maximum of PM597 in PMMA, green line (σ_a (532 nm) = 2.56·10^{-15} cm^2). The emission of the SiNOH laser is near 600 nm, red bar (σ_e (600 nm) = 0.56·10^{-15} cm^2). The laser emission is redshifted from the wavelength of maximum emission cross section at approximately 570 nm due to re-absorption of emitted photons by dye molecules in the ground state.

2.3. Design considerations

For lasers operated in sensor applications, the important characteristics are the spectrum, the polarization, the threshold, and the output power. These parameters are defined by the resonator, the properties of the laser gain medium, and the pump.

Spectrum and polarization As a gain medium, we use the organic dye Pyrromethene (PM597) dispersed in a poly(methyl methacrylate) (PMMA) matrix, see Fig. 3(d) for the associated emission and the absorption cross sections. The material offers a predominantly inhomogeneously broadened gain spectrum [32,33], which allows for simultaneous lasing of multiple longitudinal cavity modes. Note that the spectral characteristics of the modal gain of a SiNOH WG may differ from that of the dye emission cross section due to the wavelength-dependence of the modal overlap with the active cladding. In our devices, we observe lasing mostly around 600 nm, while the emission cross section peaks at around 570 nm. With a ring-shaped laser resonator, the emission spectrum of the organic laser dye is longitudinally filtered according to the comb-shaped eigenmode spectrum, having a free spectral wavelength range FSR = $\lambda_0^2 / (n_{e,g}L)$ centered at the operating wavelength λ_0, Fig. 2(c). In addition to the fundamental TE and TM mode, Figs. 2(a) and 2(b), transverse modes of higher order can propagate if the WG is sufficiently wide ($w \geq 400$ nm). For the ring resonator, we find one set of longitudinal modes for each transverse mode in each polarization. The number of lasing modes can be reduced with additional filters, see Section 4.2.

For a DFB laser, the analysis of the spectral emission characteristics relies on coupled-mode theory [31]. Assuming a DFB grating period a, the refractive index modulation along the WG can be described by an effective index modulation $n_e(z) = n_{e,av} + \Delta n_e \sin(2\beta_B z)$, having an amplitude Δn_e and an average effective refractive index $n_{e,av}$. The propagation constant is $\beta_B = 2\pi n_{e,av} / \lambda_B$ at the Bragg wavelength $\lambda_B = 2n_{e,av}a$. The coupling strength of the grating for weak coupling can then be approximated given by [31]

$$\kappa = \frac{\pi \, \Delta n_e}{\lambda_B}. \tag{3}$$

A sketch of a transmission spectrum of a DFB structure and its associated stop-band can be seen in Fig. 2(f), black line. The transmission stop-band is centered at the Bragg wavelength $\lambda_B = 2n_{e,av}a$, and the bandwidth $\Delta\lambda$ of the stop-band, Fig. 1(f), for a first-order Bragg grating is given by [31]

$$\Delta\lambda = \frac{\lambda_B^2}{\pi n_{av}} \sqrt{\kappa^2 + \frac{\pi^2}{L^2}}. \tag{4}$$

Note that, in a DFB laser without any phase shift, laser emission occurs at the stop-band edges, rather than in the center of the stop-band at λ_B, see Fig. 2(f), red dashed line. If a quarter-wavelength shift is included at the center of the Bragg-grating section, i.e., if a defect is introduced in the periodic structure, the emission wavelength can also be within the stop-band of the DFB structure. As with the ring resonator, we find one set of longitudinal modes for each transverse mode in each polarization.

Laser threshold and output power The independent estimation for the net gain at threshold, Eqs. (1) and (2), can only be applied to laser modes in media with inhomogeneously broadened gain spectrum, in which longitudinal modes do not compete for gain. For the organic gain medium used in our devices, the overall gain spectrum is predominantly inhomogeneously broadened, whereas homogeneous broadening only plays a role within very small wavelength ranges [32,33]. Within the ranges of homogeneous broadening, longitudinal modes compete for gain, and the mode with the largest net gain finally starts to oscillate. The more modes are competing, the higher the threshold for the dominant mode becomes. The two lasing modes of DFB lasers without quarter-wavelength shift are separated sufficiently so that no competition occurs. In contrast to that, the modes of ring resonators with large diameters and hence small FSR are subject to gain competition, and the lasing thresholds are therefore higher. Introducing an additional longitudinal mode filter reduces the number of longitudinal modes inside the homogeneous linewidth and decreases the pump threshold. Note that gain competition can also occur for modes of different polarizations, e.g., if TE-polarized and TM-polarized modes have a strong spatial overlap inside the gain medium, Figs. 2(a) and 2(b).

A high differential quantum efficiency η_d of the laser is important for a high output power. This is particularly important for lasers based on organic dyes, for which higher pump powers lead to a faster degradation, e.g., due to photo-oxidation, and thus reduce the lifetime of the device. The ratio of induced emission and total emission, comprising induced and spontaneous emission, is denoted as η_{ind}. The spontaneous emission depends on the total number of modes inside the emission spectrum of the material and therefore increases with the overall volume of the pumped region. The differential efficiency η_d is obtained by the product of η_{ind} and the probability that an emitted photon is coupled out of the laser cavity. This probability can be quantified by the total photon lifetime τ_P in the resonator, $\tau_P^{-1} = \tau_R^{-1} + \tau_\alpha^{-1}$, including resonator losses $\tau_\alpha^{-1} \propto \alpha$ and outcoupling loss τ_R^{-1}, where τ_R is the lifetime due to outcoupling only. The differential quantum efficiency is then given by [34, Eq. (3.151)]

$$\eta_d = \eta_{ind} \frac{1/\tau_R}{1/\tau_P}. \tag{5}$$

Low propagation loss α requires a low threshold modal gain g, Eqs. (1) and (2), and leads to a high quantum efficiency for a given outcoupling, Eq. (5). Note that the ratio η_{ind} of induced emission and total emission increases itself with τ_R. As a consequence, the outcoupling has to be optimized for extracting the maximum power from the resonator. A small active volume with a small number of modes, which can accept spontaneous emission, results in a larger η_{ind} than a larger active volume, if the overall emission is the same.

3.   Device fabrication

The SiNOH laser WG are fabricated with only one lithographical step. The WG cores are structured in a 200 nm thick stochiometric Si_3N_4 layer, which is deposited via low-pressure chemical vapor deposition (LPCVD) on top of a 2 μm thick silicon dioxide layer mechanically supported by a silicon wafer. As etch mask, we use a negative-tone resist structured by electron-beam lithography and spray developing. Dry etching with a mixture of SF_6 and CHF_3 is used to transfer the structure of the mask to the Si_3N_4 layer. An oxygen plasma etching step follows and removes the etch mask. After structuring the WG cores, a 800 nm thick layer of PMMA with dispersed laser dye Pyrromethene 597 (PM597, Radiant Dyes Laser & Accessories GmbH) is globally deposited onto the chips by spin coating to act as an active cladding. For a local deposition the gain material can be dispensed [27] or structured with electron beam or UV lithography [35]. The concentration of the dye within the PMMA matrix material is 25 μmol/ g and was optimized previously in investigations of polymer goblet lasers [35].

For characterization, the chips are cleaved on one side to provide access to the facet of the bus WG. Details of fabricated devices are shown in Fig. 3. Figure 3(a) shows a scanning electron microscopy (SEM) image of the Si_3N_4 WG cores that belong to a spiral laser with ring-resonator mode filter. To improve the pump efficiency, the ring-resonator WG is coiled up densely to form a double spiral WG with a minimal curvature radius of 40 μm in the center. Figure 3(b) displays a part of a DFB strip WG with sidewall corrugations. Figure 3(c) shows a cross-section of the Si_3N_4 WG core embedded in the dye-doped PMMA cladding.

For light emission, the structures must be optically pumped. Figure 3(d) shows the wavelength-dependent absorption and emission cross sections of PM597 dispersed in PMMA. The pump wavelength is chosen near the absorption maximum, Fig. 3(d), green vertical line, and the emission of the SiNOH laser appears near 600nm, indicated by a red bar, red-shifted from the maximum of the emission cross section of the laser dye at approximately 570 nm. This may be explained by the fact that re-absorption of emitted photons through the dye molecules in the ground state is stronger at 570 nm than at 600 nm and by a general concentration-dependence of the emission wavelength of dye lasers [36]. Emission wavelengths of approximately 600 nm have also been observed in other experiments that rely on PM597 as gain material [35,37].

4.   Characterization and demonstration of lasing

In the following, we first introduce the experimental setup used to investigate our devices. We then discuss the results obtained for spiral and DFB laser. A comparative discussion of the two device types follows in Section 5.

4.1.   Characterization setup

The experimental setup is shown in Fig. 4. The SiNOH lasers are pumped from the top by a frequency-doubled Nd:YLF pulsed laser (CL523, CrystaLaser) at a wavelength of 523 nm, a pulse duration of 20 ns, and a repetition rate of 20 Hz, Fig. 4. Pulsed operation with a rather low repetition rate was chosen to ensure relaxation of dyes in excited triplet states between subsequent pulses. The lifetime of these triplet states is typically in the microsecond range, thereby preventing operation of dye lasers at high repetition rates or in continuous-wave (cw)
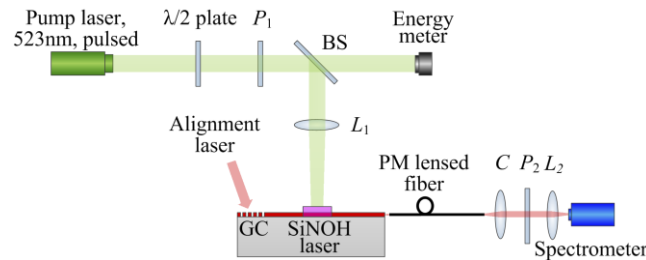
Fig. 4. Experimental setup for characterizing SiNOH lasers. The devices are pumped via a free-space beam from a pulsed laser which is focused onto the chip by a lens L_1. The energy of the pump pulsed impinging on the SiNOH devices is varied by rotating a half-wave ($\lambda/2$) plate with respect to a fixed linear polarizer P_1. A beam splitter BS transmits half of the pump emission to a pulse energy meter. The SiNOH laser emission is coupled from the chip by a lensed polarization-maintaining (PM) fiber. A collimator C and a refocusing lens L_2 are used to couple the light to a spectrometer. A rotatable linear polarizer P_2 can be inserted in the collimated portion of the beam for selecting the proper polarization of the lasing modes. The position of the lensed fiber is adjusted with the help of an auxiliary alignment laser at 635 nm, which is coupled to the bus WG (spiral laser) or to the corrugated WG (DFB laser) through a grating coupler (GC). The same grating coupler is used for measuring the transmission of the DFB structures.

mode [38,39]. The pulse energy is varied by a half-wave ($\lambda/2$) plate and a subsequent polarizer P_1, and a beam splitter BS is used to transmit half of the pump energy to an energy meter. The pump light is focused on the chip by a lens L_1. The SiNOH laser light is coupled from the chip edge with a polarization-maintaining (PM) lensed fiber. A collimator C and a refocusing lens L_2 are used to couple the emitted light to a spectrometer (Shamrock 500i, Andor, 60 pm resolution, 2 s integration time). An optional rotatable linear polarizer P_2 is inserted between the fiber collimator and the refocusing lens for selecting the proper polarization of the lasing mode. An auxiliary alignment laser and a grating coupler help in actively adjusting the lensed fiber to the output WG of the SiNOH laser. For the DFB structures, we also measure the transmission by coupling the light of a white-light source (SuperK, NKT Photonics) to the chip via the grating coupler and by capturing the transmitted light at the output with the lensed fiber which is connected to the spectrometer.

All experiments reported in the following were conducted at room temperature. However, we expect that SiNOH lasers can be operated at other temperature ranges as well. Previous experiments using also PM597-doped PMMA as a gain material have shown that lasing is still possible at temperatures of 65 °C [35]. This should be sufficient for biophotonic experiments, which are usually conducted at room temperature or at body temperatures around 37 °C. Cooling organic dyes to below 0 °C can even improve the emission performance [40].

4.2. Lasers based on spiral-shaped ring resonators

The ring resonator has a perimeter of $2L = 17.5$ mm and consists of a densely packed double spiral for optimally filling the pump spot area, see Figs. 5(a)–5(c) for a sketch of the device layout. The pump beam has a Gaussian profile with a full-width half-maximum spot size of 200 µm. The curvature of the spiral-shaped WG is limited to provide a minimum bending radius of 40 µm, thereby keeping the associated loss sufficiently low. To achieve low propagation loss for the fundamental TE and TM modes, the WG width is chosen to be 500 nm, leading to two guided modes for each polarization at a wavelength of 600 nm. The multimode (MM) sections are indicated by black lines in Figs. 5(a)–5(c). Measuring the transmission of the straight MM WG sections using an undoped PMMA cladding without laser dye, we find a

propagation loss of 5 dB/cm. This is much lower than the loss of 7 dB/cm found for narrower, 300 nm-wide single-moded WG with undoped PMMA cladding. We believe that these losses can be further reduced by optimized fabrication processes. To suppress laser oscillation of higher order transverse modes in the MM devices, we use short single-mode WG sections, indicated as orange lines in Figs. 5(a)–5(c), which are inserted in the center of the spiral and as a loop in the coupling section between spiral and straight bus WG. As a consequence, we find significantly reduced lasing thresholds for lasers with MM WG in the spiral section as compared to their single-mode counterparts – despite the slightly reduced overlap of the guided light with the active cladding in the MM WG. Note that significantly smaller propagation losses could be achieved by optimized fabrication processes, which should allow for further reductions of the lasing threshold.

In a first step of our device characterization, we measure the lasing threshold of the double spiral laser with a simple loop at the outer end of the spiral WG, Fig. 5(a). In this experiment, the whole spiral WG is pumped with a beam having a Gaussian intensity distribution, see green spot in Fig. 5(a). This pump spot overlaps only partially with the spiral WG such that much of the pump energy remains unused. Figure 5(d) shows the normalized lasing spectrum for a pump pulse energy of 715 nJ, recorded with an integration time of 2 s of the CCD camera in the spectrometer. The FSR of the spiral-shaped ring is estimated to be $\text{FSR}_{\text{Spiral}} = 10$ pm, which corresponds to 8.3 GHz and cannot be resolved by the spectrometer (resolution 60 pm). The recorded spectra are not very stable – lasing occurs only in a small range (590 nm to 610 nm) of the spontaneous emission spectrum of the laser dye, and the center of the lasing spectrum changes from integration interval to integration interval. We attribute this to mode competition, possibly in combination with temperature-induced phase fluctuations of mode patterns in the multi-mode spiral WG. Note that the spectrometer used for recording the emission spectra is not calibrated and indicates only relative power levels P/P_0 with respect to an unknown reference power P_0. This reference power is the same for all measurements reported in the subsequent experiment, such that relative power levels P/P_0 may be compared across different measurements. For quantifying the input/output power characteristics of our devices, we sum up the powers in all spectral lines and depict the calculated normalized output power P/P_0 as a function of the pump pulse energy W, Fig. 5(g). Despite the unstable lasing spectrum, no significant fluctuation of the total emitted power is observed which supports the idea of mode competition. We find a laser threshold of 312 nJ, corresponding to a pump fluence of approximately $400\mu\text{J}/\text{cm}^2$ for the area occupied by the spiral WG.

In a next step, we investigate a spiral laser, where the outer ends of the double spiral are optically connected through a small ring resonator, Fig. 5(b). This ring resonator has a free spectral range of $\text{FSR}_{\text{Ring}} = 660$ pm (540 GHz) and is used as longitudinal mode filter. We again use a Gaussian pump spot covering the entire spiral WG, having the same overlap with the spiral WG as in the previous experiment. Figure 5(e) shows the lasing spectrum for a pump pulse energy of 87 nJ. Lasing occurs for the fundamental TM mode (blue) and for the fundamental TE mode (red). The emission lines are spaced by multiples of FSR_{Ring} The spectrum differs greatly from Fig. 5(d) and is stable from integration interval to integration interval. We attribute this to the fact that the homogeneous linewidth of the dye is comparable to or smaller than FSR_{Ring} such that different longitudinal modes do not compete for gain. As a consequence, the pump energy at threshold, Fig. 5(h), is smaller than for the case of modes competing for gain as in Figs. 5(a), 5(d) and 5(g). Figure 5(h) shows further that TM-polarized lasing modes have lower thresholds (53 nJ) than TE-polarized modes (60 nJ), corresponding to pump fluences of $56\mu\text{J}/\text{cm}^2$(TM) and $65\mu\text{J}/\text{cm}^2$(TE) at the laser-active area of the spiral, respectively. This is attributed to the fact that TM-polarized modes transport a larger fraction (0.2) of cross-sectional power in the gain medium outside the WG core than the TE modes (0.17). In addition, the loss for a TM-polarized mode (high electric field strengths at the smooth upper surface) is smaller than for a TE-polarized mode (high electric field strengths at the rough sidewalls). Moreover, the differential quantum
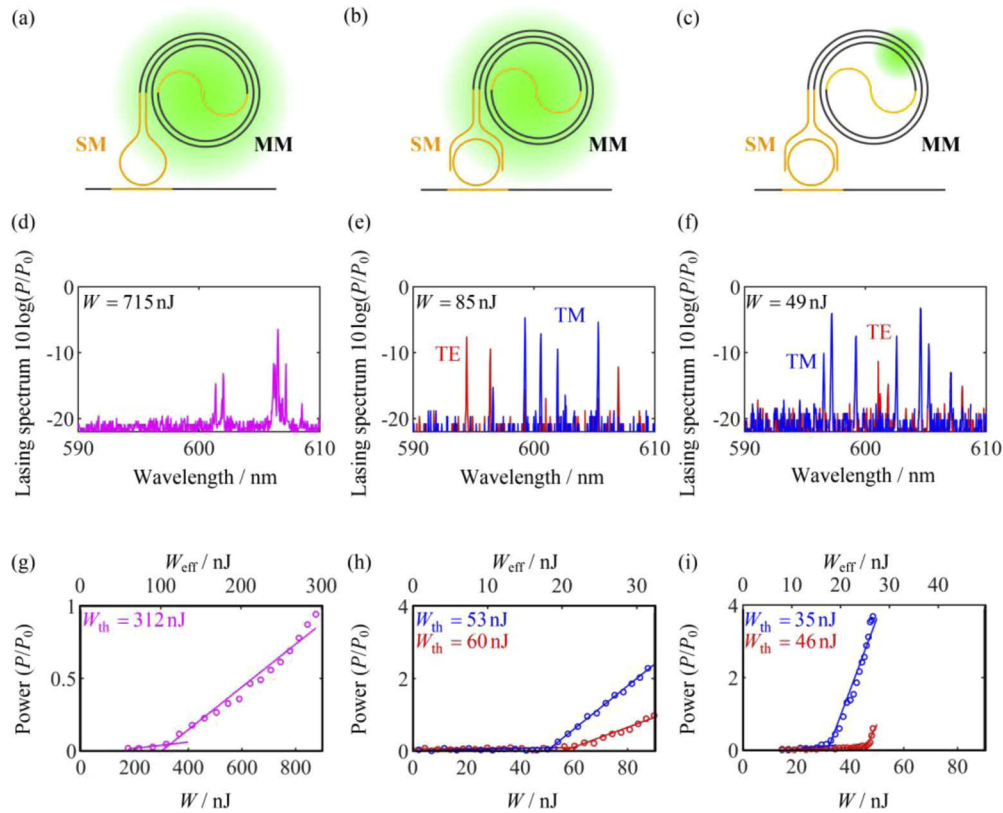
Fig. 5. Characterization of spiral SiNOH lasers using different mode filters and pump spot sizes. (a)–(c) Resonator geometries and pump spots (green). A transverse mode filter (orange) is implemented by tapering down the multimode spiral-shaped resonator WG from 500 nm width to 300 nm for single-mode propagation. (b),(c) A ring resonator with a round-trip propagation loss of 1 dB (4 dB /cm, $Q = 5 \times 10^3$) acts as a longitudinal mode filter at the outer end of the double spiral and reduces the number of lasing modes in the spiral resonator. A pump spot size of the order of the spiral diameter leads to a waste of pump energy that is absorbed outside the overlap region with the spiral WG, see Subfigures (a),(b). Focusing the pump spot to an area with high WG density, Subfigure (c), decreases the threshold. (d)–(f) Emission spectra. Since the spectrometer used for recording the emission spectra is not calibrated, we report the output power with respect to a common reference power P_0. Note that the scaling of the vertical axis in Subfigure (d) differs from that in Subfigures (e) and (f). If a small ring resonator is used as a longitudinal mode filter at the outer end of the double spiral, its FSR determines the lasing lines. (g)–(i) Laser output power as a function of the total pump pulse energy W (lower horizontal axis) and of the effective pump pulse energy W_{eff} that is absorbed in the overlap region of the respective pump spot with the spiral WG (upper horizontal axes). The threshold energies W_{th} refer to the total pump pulse energy, i.e., to the lower axes. In Subfigure (g), the scaling of the axes differs from the scaling in Subfigures (h) and (i). We find that introducing the additional ring filter as spectrally selective feedback, Subfigure (h), decreases the pump threshold by a factor of 6 compared to the case without ring filter, Subfigure (g). Using a focused pump spot that leads to an enhanced overlap with the spiral WG, Subfigure (i), we can achieve a further reduction of the threshold by a factor of 1.5 along with an increase of the differential quantum efficiency, to be seen by the steeper slope of the laser characteristic as compared to Subfigure (h).

efficiency increases significantly when introducing the filter ring resonator. This can be seen by comparing the slopes in Figs. 5(g) and 5(h) (note the different scales on the vertical axes). To understand this result, it is important to note that the power coupling factor between the loop and the straight outcoupling WG in Fig. 5(a) is the same as the power coupling factor between the ring and the straight outcoupling WG in Fig. 5(b). However, the resonant power enhancement in the filter ring leads to an effective increase of power coupled from the spiral to the straight output WG, thereby causing a significant reduction of the outcoupling photon lifetime τ_R of the laser cavity. Since both structures in Fig. 5(a) and Fig. 5(b) feature the same propagation losses in the spiral and hence the same photon lifetime τ_α, a reduction of τ_R leads to an increase of the differential quantum efficiency η_d, see Eq. (5).

The threshold of the spiral laser can be further decreased by increasing the overlap of the pump spot with the spiral WG. One way to achieve this is to focus the pump spot to an area with densely spaced WG, Fig. 5(c), green spot, such that a larger fraction of pump light is absorbed in the vicinity of the Si_3N_4 WG. The emission spectrum obtained with the focused pump spot, Fig. 5(f), shows similar properties as the one obtained by pumping the entire spiral with a large pump spot, Fig. 5(e). At the same time, the focused pump spot allows to reduce the overall pump pulse energy at the lasing threshold, Fig. 5(i). Specifically, we obtain a threshold pump pulse energy of 46 nJ and 35 nJ for the TE and the TM mode, respectively, and the corresponding fluences amount to $1095\mu J/cm^2$ and $980\mu J/cm^2$. This is a reduction by a factor of 1.5 as compared to the case of the large pump spot, see Fig. 5(h). For a fair comparison of different pump spot geometries, we define an effective pump pulse energy W_{eff} that is absorbed in the overlap region of the pump spot and the spiral WG, see upper horizontal axes in Figs. 5(g), 5(h), and 5(i). The area of the spiral was modeled as a ring with a width of 50 µm and an inner radius of 80 µm for the densely spaced WG regions. The S-shaped bend in the middle of the spiral is neglected since it does not play a significant role.

Comparing Figs. 5(h) and 5(i), we find that the effective pump pulse energy W_{eff} is the same for both cases, and is in accordance with Fig. 3(d), indicating that the re-absorption in the unpumped regions is small. However, the differential quantum efficiency is larger for the focused pump beam, because the active volume is smaller and η_{ind} is therefore larger, see text after Eq. (5).

We also estimate the total output power levels that can be achieved with the current devices. To this end, we use a spiral laser according to Fig. 5(b), and we exchange the spectrometer with the pulse energy meter, see Fig. 4. For a pump pulse energy of $W = 4\mu J$, we measure an emitted pulse energy of 80 pJ at the fiber output. This corresponds to an on-chip pulse energy of approximately 1 nJ when accounting for a fiber-chip coupling loss of the order of 9 dB and for an on-chip propagation loss of 2 dB in the 3 mm-long passive WG between the laser and the chip edge. For a pulse duration of approximately 20 ns, this corresponds to a pulse peak power of the order of 50 mW. Clearly, the average power is much lower and amounts to approximately 20 nW for the 20 Hz pulse repetition frequency used in our experiment. We believe that the output power of our SiNOH lasers can be greatly improved by optimized device design, material composition, and fabrication processes. In addition, the average power can be increased by using higher pulse repetition rates – probably in combination with shorter pulse durations to keep the photodegradation low, see Section 5.

While the gain spectrum of the dyes in the active organic cladding is predominantly subject to inhomogeneous gain broadening, homogeneous broadening might play a role as well [32,33]. This can also be observed from the emission spectra of the SiNOH spiral lasers: The filter ring in Figs. 5(b) and 5(c) has a free spectral range of FSR = 0.6 nm. When pumping the full ring, Fig. 5(b), laser emission occurs only for cavity modes that are spaced by at least two FSR, see corresponding spectrum in Fig. 5(e). On the other hand, when pumping only a part of the ring, Fig. 5(c), cavity modes spaced by one FSR may oscillate, but exhibit a strong imbalance in emitted power. We attribute both findings to gain competition within a partially homogeneously

broadened gain spectrum, where the bandwidth of the homogeneous broadening is of the order of 0.6 nm, corresponding to one FSR.

4.3.　Distributed-feedback laser

Sidewall corrugations of a WG can couple counter-propagating WG modes and thereby establish a distributed feedback (DFB) resonator, Fig. 6(a). The DFB structure is defined by its length L, width w, corrugation depth d, and corrugation period a. The number of periods is denoted by m, the feedback strength is κ, Eq. (3), and the separation of the lowest-order lasing modes is $\Delta\lambda$, Eq. (4). The active medium of the DFB laser is pumped from the top with an elliptical pump spot that fully illuminates the DFB WG.

Figure 6(b), black line, shows the typical transmission spectrum of a passive DFB resonator measured by coupling the light of a super-continuum laser (SuperK Versa, NKT Photonics GmbH) to the GC and by detecting the transmitted light with the spectrometer, Fig. 4. The resolution bandwidth (RBW) has been chosen to rather high RBW = 260 pm because the super-continuum source is limited in power spectral density. As a consequence, the transmission maxima expected at the band edges cannot be resolved. The emission spectrum of the pumped resonator is depicted in the same figure by a red line and shows two lasing modes TE_{lo} and TE_{up} having a spectral distance of $\Delta\lambda = 1.2$nm. The dominant mode occurs at the lower bandgap edge for lower photon energies, TE_{lo}, whereas the lasing mode TE_{up} at the upper high-photon-energy bandgap edge is less pronounced. Note that when pumping the laser, the induced gain and the higher temperature lead to a blue shift of the DFB stop-band as compared to the cold resonator. For better visualization, this was compensated by blue-shifting the measured transmission spectrum by 0.2 nm in Fig. 6(b).

The laser output powers P_{lo} and P_{up} for the two lasing modes in Fig. 6(b) was measured as a function of the pump pulse energy W, Fig. 6(c). In the investigated device, the dominant laser mode of Fig. 6(b), filled red circles, starts lasing for lower pump pulse energies $W_{th,lo} = 32$nJ than the less pronounced one with $W_{th,up} = 41$nJ, open red circles. The differential quantum efficiency according to Eq. (5) is larger for the TE_{lo} mode than for the TE_{up} mode. Note that this behavior was not systematic, and that we also observed DFB lasers or pump conditions in which the laser emission at the lower stop-band edge was equal to or stronger than the emission at the upper edge. We attribute this observation to slight imbalances in the net gain of the two modes that may be caused by, e.g., different overlaps with the gain material, by differences in scattering losses due to rough wave WG surfaces, or by frequency-dependent external feedback originating from the remote wave WG facets. As both modes are amplified, the homogeneous line broadening of the dye must be smaller than the spectral separation of the DFB resonator modes.

Figure 6(d) shows transmission spectra for TE (red lines) and TM modes (blue lines) of DFB resonators with different corrugation depths d but otherwise same geometries. The center wavelengths of the stop-bands for TE modes are red-shifted by 16 nm . . . 18 nm from those of the TM-polarized modes, which is caused by the slightly higher effective index seen by the TE modes as compared to the TM modes. At the same time, we observe a red-shift of the stop-bands for increasing depths d. This red-shift is slightly stronger for the TE-polarized modes than for their TM-polarized counterparts. This can be explained by the following consideration: Changing the corrugation depth does not only change the coupling strength κ, but also the average WG width $w_{e,av} = w + d/2$. This leads to an increase of the average effective refractive index $n_{e,av}$ seen by the guided modes, and this increase is stronger for TE polarization than for TM. As a consequence, the center wavelength $\lambda_B = 2n_{e,av}a$ increases stronger for TE than for TM modes. We also find that the bandwidth $\Delta\lambda$ of the stop-band is slightly larger for TM-polarized modes than for TE polarized modes for the same corrugation depth d, which means that the grating strength is larger for TM modes.

The threshold pump pulse energies measured for devices with different coupling strengths κ and different lengths $L = ma$ are shown in Fig. 6(e), where TM polarization is indicated by blue circles and TE polarization by red circles. For better comparison of the threshold pump energies we consider again only the effective pump pulse energy $W_{\text{th,eff}}$ that is absorbed in the vicinity of the DFB resonator, i.e., within a rectangular region that comprises the DFB WG and as well as a 600 nm-wide strip to each side of the WG. In this graph, the coupling strength κ was obtained from simulations of homogeneous WG with widths w and $w + d$, which provides the effective-index difference Δn_{e} and the coupling strength κ according to Eq. (3). For comparing the experimental results to the theory developed in [31], we also plot dashed and solid reference lines in Fig. 6(e). These lines are obtained by assuming that the gain at threshold is proportional to the associated pump pulse energy, $W_{\text{th,eff}} \propto g_{\text{th}}L$.

In the low-gain regime, i.e., in the right-hand part of the diagram ($g_{\text{th}} \ll \kappa$), we use Eq. (2) to derive a model function. For simplicity, we assume that the gain at threshold is mainly dictated by the finite feedback of the DFB structure while the impact of the propagation loss α can be neglected, i.e., $\alpha L \ll 2(\pi / \kappa L)^2$ even in the low-gain regime. This leads to a model function of the form $W_{\text{th,eff}} = C (\pi / \kappa L)^2$, where the scaling factor C is used as a fit parameter. The associated sections of the reference curves in the right-hand part of Fig. 6(e) are drawn as solid lines. For the high-gain regime, $g_{\text{th}} \gg \kappa$, Ref. [31] only provides a numerical solution [31, Fig. 8], which we plot into the left-hand part of Fig. 6(e) as solid lines using the scaling factor C obtained from the low-gain regime. A dashed spline connects the two partial curves.

Even though the measured data points in Fig. 6(e) are subject to substantial variations, they follow the overall trend obtained from the reference lines. The laser threshold decreases for larger κL, and the threshold is smaller for TM polarization than for TE polarization. This can be explained by the larger overlap of the TM-polarized mode with the gain medium compared to the TE-polarized mode. In addition, the propagation loss is expected to be smaller for TM-polarized modes as large field strengths are located at the smooth upper surface of the WG core, whereas TE-polarized modes interact stronger with the rather rough sidewalls of the WG core. Low thresholds of $W_{\text{th,eff}} < 0.3$ nJ are reached with total coupling strengths $\kappa L > 15$. The pump fluences on the resonator at threshold are $40 \mu\text{J} / \text{cm}^2 \ldots 60 \mu\text{J} / \text{cm}^2$. Note that, when designing DFB lasers, decreasing the threshold by increasing κL is only effective to a certain extent. At very large values of κL, the optical feedback is very strong, and the outcoupling rate τ_{R}^{-1} becomes small compared to the overall resonator loss rate τ_{P}^{-1}, thereby reducing the differential quantum efficiency according to Eq. (5).

To achieve single-mode lasing, DFB lasers with a quarter-wave shift (DFB$_{\lambda/4}$) at $z = L / 2$ were investigated, see Fig. 7(a). The optical quarter-wave ($\lambda / 4$) shift in the center of the Bragg grating corresponds to a spatial shift of the z-dependent width modulation by half the grating period, i.e., by $a / 2$. This leads to laser emission at the Bragg wavelength λ_{B}, supported by a lasing mode that is spatially confined to the region of the phase shift and that decays exponentially towards both ends of the grating. Figure 7(b), black line, shows the transmission spectrum of a passive DFB$_{\lambda/4}$ resonator with the parameters given in Fig. 7(a), which leads to $\kappa L = 3.4$. Also here, the transmission spectrum was measured using a rather high RBW of 260 pm to cope with the limited output power of the super-continuum source.

The emission spectrum of the pumped resonator is depicted in the same figure, red line, recorded with a RBW of 60 pm. From a Lorentzian fit, we calculate the full-width half-maximum of the lasing emission to be FWHM = 230 pm (190 GHz). Although there is no characteristic transmission peak at λ_{B} in the middle of the transmission stop-band, a laser mode emerges at λ_{B}. We attribute the missing transmission peak to the non-negligible background in the transmission measurement and to the limited spectral resolution, which was again dictated by the limited emission power of the white-light source. The laser output power was measured as a function of the overall and the effective pump pulse energy W and W_{eff}, respectively, Fig. 7(c). The effective
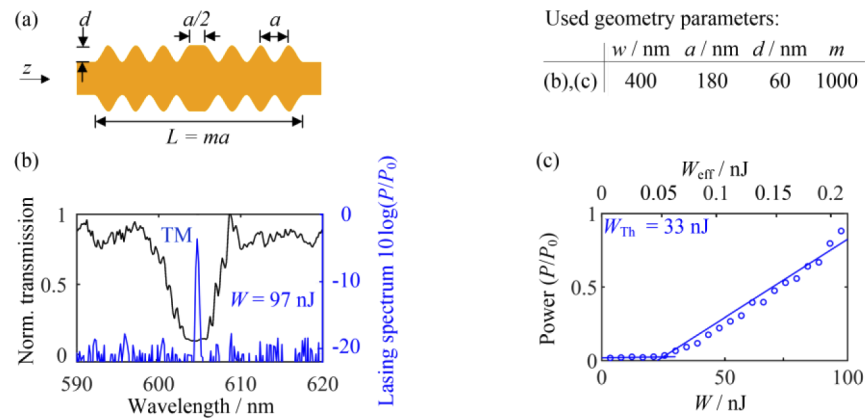
Fig. 6. Transmission spectrum and threshold of a $\text{DFB}_{\lambda/4}$ laser. (a) Schematic of a DFB section with quarter-wave ($\lambda/4$) shift at $z = L/2$, total length L, corrugation depth d, period a, and width w. The quarter-wave ($\lambda/4$) shift corresponds to a geometrical shift by $a/2$ and leads to lasing at the Bragg wavelength. Parameters for Figs. 6(b) and 6(c) are listed in the table on the right. (b) Normalized transmission spectrum (black line, RBW = 210 pm) and laser emission (blue line, RBW = 60 pm) for a TM-polarized mode. The lasing mode is located at λ_B in the middle of the stop-band. The expected transmission peak at λ_B cannot be seen, due to a non-negligible background and due to limited spectrometer resolution and low emission power of the whit-light source used for the measurement. (c) Laser characteristics: The TM laser mode starts lasing for pump pulse energies $W_{th} = 33$ nJ. The horizontal upper axis shows the fraction of the pump pulse energy W_{eff} that is absorbed in the overlap region with the $\text{DFB}_{\lambda/4}$ structure. The output power is again specified with respect to a common reference power P_0.

pump pulse energy W_{eff} refers again to the pulse energy absorbed in the vicinity of the DFB resonator, i.e., within a rectangular region that comprises the DFG WG and a 600 nm-wide strip to each side of the WG.

We find a threshold of $W_{th} = 33$nJ ($W_{th,eff} = 0.07$nJ), which is comparable to the threshold of the DFB gratings with large κL in Fig. 6(d). The threshold pump fluence at the resonator is $64\mu\text{J}/\text{cm}^2$.

5. Comparative discussion

Based on our analysis of the different SiNOH laser concepts we compare the properties that are crucial for applications in bio-sensors. Important requirements are the spectral properties of the emitted light, the on-chip footprint, as well as robustness and tolerance with respect to fabrication inaccuracies. These aspects are discussed in the following section.

Spectral properties of emitted light For the spiral resonators, the number of modes is mainly defined by the FSR of the feedback filter ring, the spectral distribution of the net gain, and the bandwidth of the homogeneous line broadening. In our experiments, we found that lasing occurs within a 15 nm bandwidth centered at approximately 600 nm. The number of modes within the bandwidth can be controlled by the radius of the feedback filter ring. Increasing the FSR to obtain lasing in a single longitudinal mode is not always possible because smaller radii of the feedback ring filter can lead to higher losses due to radiation and therefore to higher thresholds. Moreover, the exact emission wavelength might sensitively depend on the temperature of the feedback ring filter. For spiral lasers, lasing can occur simultaneously in TE and TM polarization.

For the DFB resonator, single-mode emission can be achieved over a large spectral range, limited by the gain spectrum of the dye. By carefully choosing the period of the grating, the

polarization can be controlled. In some cases, two modes can be amplified at both boundaries of the stop-band, but usually one mode is dominant. For DFB$_{\lambda/4}$ lasers, only one mode at the Bragg wavelength oscillates. Similar to the DFB lasers, the mode can be chosen in a large spectral range by varying the period of the grating. For both DFB and DFB$_{\lambda/4}$ lasers, emission usually occurs in one polarization only.

Device lifetime Generally, the device lifetime of organic lasers is limited by photodegradation of the dyes [38]. However, this did not represent a practical limitation in our experiments – we could test the SiNOH devices for several hours, i.e., with more than 100 000 pump pulses, while still retaining at least 50% of the initial emission power. These findings are in line with recently published results on similar devices [28] and should permit operation of SiNOH lasers in disposable point-of-care devices. Note that the pump pulse duration used in our experiments amounts to 20 ns and is thus significantly longer than the fluorescence lifetime of the dyes, which is approximately 5 ns [41]. Using shorter pump pulses might hence allow to further improve the device lifetime [38,39].

We also observe an increase of the degradation rate if the pump spot is focused to a smaller area as in the scheme depicted in Fig. 5(b). This can be explained by considering the photodegradation mechanism in more detail: When photons are absorbed, the dye molecules are transferred from a singlet ground state to a singlet excited state, which has a lifetime in the nanosecond range [42]. With a certain probability, such a singlet excited state can undergo an intersystem crossing to a triplet excited state, which requires another intersystem crossing to relax to the singlet ground state and which thus has a rather long lifetime in the microsecond range [42]. Photodegradation can either directly result from a chemical reaction of excited triplet-state dyes with their molecular environment [43] or can be indirectly caused through generation of highly reactive singlet oxygen molecules during one of the intersystem crossings [44]. Focusing the pump to a smaller cross section has two effects on this mechanism: First, the length of the active WG sections within the pump spot is smaller, such that laser operation requires a higher density of excited single-state dyes to compensate the cavity losses. Second, a higher photon density may also lead to further transitions from the first excited singlet states to higher singlet states, from where the transition to a triplet state is more likely [44]. We believe that a systematic investigation of these effects can lead to additional approaches to increase the device lifetime.

Footprint and overlap with pump spot The larger the overlap of the laser WG with the pump spot, the more energy can be transferred to the SiNOH laser. For spiral lasers, good overlap with a circular pump spot can be achieved and can be further increased by focusing the pump light to an area with densely spaced WG or by using alternative pump spot shapes such as rings. Generally, spiral lasers have larger on-chip footprint than other devices.

For the DFB and the DFB$_{\lambda/4}$ laser, the overlap with a circular pump spot is much smaller than that for the spiral, but its size may be increased by using, e.g., a cylindrical lens that generates a line-shaped focus. The devices offer small on-chip footprint and lend themselves to integration in arrays which can be excited by one large pump spot.

Robustness and tolerance to fabrication inaccuracies Within the limited set of approximately 50 devices investigated for the current study, we found the reliability of spiral lasers to be higher than that of DFB and DFB$_{\lambda/4}$ lasers, especially when the devices are coupled to additional on-chip photonic circuits. This could be caused by optical feedback, which might have a higher impact on DFB and DFB$_{\lambda/4}$ lasers than on spirals, or by a higher sensitivity of the DFB gratings with respect to fabrication inaccuracies. These aspects require further investigation.
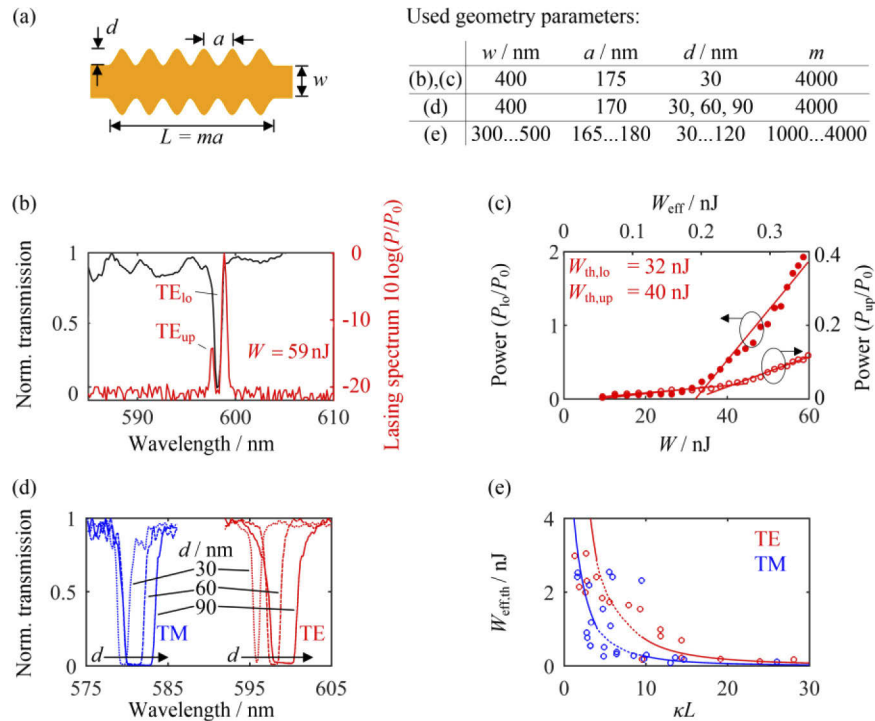
Fig. 7. Transmission spectra and threshold characteristics of DFB resonators with various geometries. (a) Schematic of a DFB section with length L, corrugation depth d, period a, and width w along with the parameters used in Figs. 6(b)–6(e). (b) Normalized transmission spectrum of the DFB WG (black line, RWB = 260 pm) and normalized lasing spectrum (red line, RBW = 60 pm) of a DFB laser above threshold. The lasing modes are located at the edges of the stop-band which are blurred in the measured transmission spectrum because of the rather coarse resolution of the spectrometer. The dominant laser mode occurs at the low-frequency stop-band edge TE_{lo}, i.e., at higher wavelengths, whereas the lasing mode at the upper stop-band edge TE_{up} (higher frequency, lower wavelength) has much less power. (c) Laser characteristics: The dominant laser mode TE_{lo} at the lower stop-band edge starts lasing for lower pump pulse energies (•, $W_{th,lo} = 32$ nJ, left vertical axis) than the weak mode TE_{up} at the upper stop-band edge (○, $W_{th,up} = 41$ nJ, right axis). The horizontal upper axis gives effective pump pulse energy W_{eff}, defined by the fraction of the pump pulse energy that is absorbed in the overlap region with the DFB structure. Since the spectrometer used for recording the emission spectra is not calibrated, we report the output power with respect to a common reference power P_0. (d) Normalized transmission spectrum of the DFB WG for TE (red lines) and TM polarization (blue lines) for different corrugation depths d. A larger corrugation depth d leads to a larger stop-band width $\Delta\lambda$. For the same corrugation depth d, $\Delta\lambda$ is larger for TM than for TE polarization. (e) Threshold pump pulse energies for different coupling strengths κL for TE and TM polarization. The pump pulse energy W_{eff} refers to the effective pulse energy that is absorbed in the vicinity of the DFB WG structure. The laser threshold decreases for larger κL. For TM polarization, we observe smaller thresholds than for TE polarization. This can be explained by the larger overlap of the TM mode with the gain medium and by the smaller propagation loss compared to the TE mode.

6. Summary

We demonstrate and investigate hybrid organic dye lasers emitting at 600 nm wavelength that can be monolithically integrated on the silicon nitride (Si_3N_4) platform. The Si_3N_4-organic hybrid

(SiNOH) lasers are operated by optical pumping from the top with relaxed alignment precision of the pump spot with respect to the on-chip structures. SiNOH lasers can be fabricated in a single lithography step by structuring the silicon nitride waveguides together with other devices on the same chip, and by subsequently dispensing or spin coating the organic gain medium on top of the WG cores.

In our proof-of-concept study, we investigate two different laser geometries, spiral-shaped ring resonators and DFB resonators, and compare our experimental findings with theoretical models. All investigated SiNOH lasers offer acceptable threshold fluences of $40\,\mu J/cm^2 \ldots 70\,\mu J/cm^2$ with vast room for further improvement. We also provide a comparative discussion of the different device concepts. To the best of our knowledge, our experiments represent the first demonstration of SiNOH spiral lasers and of SiNOH DFB-lasers with first-order gratings. By using different dyes and by adapting the resonator design, SiNOH lasers should be able to address the entire visible wavelength range. We expect that the versatility of the device concepts, the simple operation principle and the compatibility with cost-efficient mass fabrication will make the SiNOH lasers a highly attractive option for applications in bio-photonics and point-of-care diagnostics.

Disclosures

The authors declare no conflicts of interest.

References

1. E. Makarona, P. Petrou, S. Kakabakos, M. Misiakos, and I. Raptis, "Point-of-need bioanalytics based on planar optical interferometry," Biotechnol. Adv. **34**(3), 209–233 (2016).
2. E. Luan, H. Shoman, D. M. Ratner, K. C. Cheung, and L. Chrostowski, "Silicon photonic biosensors using label-free detection," Sensors **18**(10), 3519 (2018).
3. P. Muellner, E. Melnik, G. Koppitsch, J. Kraft, F. Schrank, and R. Hainberger, "CMOS-compatible Si₃N₄ waveguides for optical biosensing," Procedia Eng. **120**, 578–581 (2015).
4. A. Z. Subramanian, E. Ryckeboer, A. Dhakal, F. Peyskens, A. Malik, B. Kuyken, H. Zhao, S. Pathak, A. Ruocco, A. De Groote, P. Wuytens, D. Martens, F. Leo, W. Xie, U. D. Dave, M. Muneeb, P. Van Dorpe, J. Van Campenhout, W. Bogaerts, P. Bienstman, N. Le Thomas, D. Van Thourhout, Z. Hens, G. Roelkens, and R. Baets, "Silicon and silicon nitride photonic circuits for spectroscopic sensing on-a-chip," Photonics Res. **3**(5), B47–B59 (2015).
5. J.-C. Tinguely, Ø. I. Helle, and B. S. Ahluwalia, "Silicon nitride waveguide platform for fluorescence microscopy of living cells," Opt. Express **25**(22), 27678 (2017).
6. K. F. Palmer and D. Williams, "Optical properties of water in the near infrared," J. Opt. Soc. Am. **64**(8), 1107–1110 (1974).
7. H. W. Lim and N. A. Soter, *Clinical photomedicine* (Dekker, 1993).
8. P. Muñoz, G. Micó, L. A. Bru, D. Pastor, D. Pérez, J. D. Doménech, J. Fernández, R. Baños, B. Gargallo, R. Alemany, A. M. Sánchez, J. M. Cirera, R. Mas, and C. Domínguez, "Silicon nitride photonic integration platforms for visible, near-infrared and mid-infrared applications," Sensors **17**(9), 2088 (2017).
9. D. J. Blumenthal, R. Heideman, D. Geuzebroek, A. Leinse, and C. Roeloffzen, "Silicon nitride in silicon photonics," Proc. IEEE **106**(12), 2209–2231 (2018).

10. G. M. Huffman, C. Brodnik, S. Pinho, D. Gundavarapu, D. J. Baney, and Blumenthal, "Integrated resonators in an ultralow loss Si$_3$N$_4$/SiO$_2$ platform for multifunction applications," IEEE J. Sel. Top. Quantum Electron. **24**(4), 1–9 (2018).

11. W. D. Sacher, J. C. Mikkelsen, Y. Huang, J. C. C. Mak, Z. Yong, X. Luo, Y. Li, P. Dumais, J. Jiang, D. Goodwill, E. Bernier, P. G.-Q. Lo, and J. K. S. Poon, "Monolithically integrated multilayer silicon nitride-on-silicon waveguide platforms for 3-D photonic circuits and devices," Proc. IEEE **106**(12), 2232–2245 (2018).

12. H. R. Philipp, "Optical properties of silicon nitride," J. Electrochem. Soc. **120**(2), 295–300 (1973).

13. I. H. Malitson, "Interspecimen comparison of the refractive index of fused silica," J. Opt. Soc. Am. **55**(10), 1205–1209 (1965).

14. M. Daimon and A. Masumara, "Measurement of the refractive index of distilled water from the near-infrared region to the ultraviolet region," Appl. Opt. **46**(18), 3811–3820 (2007).

15. J. Wang, Z. Yao, and A. W. Poon, "Integrated optofluidic label-free biosensors using a silicon-nitride-based coupled-resonator optical waveguide," Proc. SPIE **9750**, 975014 (2016).

16. T. Taniguchi, A. Hirowatari, T. Ikeda, M. Fukuyama, Y. Amemiya, A. Kuroda, and S. Yokoyama, "Detection of antibody-antigen reaction by silicon nitride slot-ring biosensors using protein G," Opt. Commun. **365**, 16–23 (2016).

17. E. S. Hosseini, J. D. B. Purnawirman, J. Bradley, G. Sun, T. N. Leake, D. D. Adam, M. R. Coolbaugh, and Watts, "CMOS-compatible 75 mW erbium-doped distributed feedback laser," Opt. Lett. **39**(11), 3106–3109 (2014).

18. J. T. Bovington, M. J. R. Heck, and J. E. Bowers, "Heterogeneous lasers and coupling to Si$_3$N$_4$ near 1060 nm," Opt. Lett. **39**(20), 6017–6020 (2014).

19. M. Belt and D. J. Blumenthal, "Erbium-doped waveguide DBR and DFB laser arrays integrated within an ultra-low-loss Si$_3$N$_4$ platform," Opt. Express **22**(9), 10655–10660 (2014).

20. Y. Chen, H. D. TBucio, A. Z. Khokhar, M. Banakar, K. Grabska, F. Y. Gardes, R. Halir, Í. Molina-Fernández, P. Cheben, and J.-J. He, "Experimental demonstration of an apodized-imaging chip-fiber grating coupler for Si$_3$N$_4$ waveguides," Opt. Lett. **42**(18), 3566–3569 (2017).

21. Y. Zhu, W. Xie, S. Bisshop, T. Aubert, E. Brainis, P. Geiregat, Z. Hens, and D. van Thourhout, "On-chip single-mode distributed feedback colloidal quantum dot laser under nanosecond pumping," ACS Photonics **4**(10), 2446–2452 (2017).

22. P. J. Cegielski, S. Neutzner, C. Porschatis, H. Lerch, J. Bolten, S. Suckow, A. R. S. Kandada, B. Chmielak, A. Petrozza, T. Wahlbrink, and A. L. Giesecke, "Integrated perovskite lasers on a silicon nitride waveguide platform by cost-effective high throughput fabrication," Opt. Express **25**(12), 13199–13206 (2017).

23. P. J. Cegielski, A. L. Giesecke, S. Neutzner, C. Porschatis, M. Gandini, D. Schall, C. A. R. Perini, J. Bolten, S. Suckow, S. Kataria, B. Chmielak, T. Wahlbrink, A. Petrozza, and M. C. Lemme, "Monolithically integrated perovskite semiconductor lasers on silicon photonic chips by scalable top-down fabrication," Nano Lett. **18**(11), 6915–6923 (2018).

24. W. Xie, T. Stöferle, G. Rainò, T. Aubert, S. Bisschop, Y. Zhu, R. F. Mahrt, P. Geiregat, E. Brainis, Z. Hens, and D. van Thourhout, "On-chip integrated quantum-dot–silicon-nitride microdisk lasers," Adv. Mater. **29**(16), 1604866 (2017).

25. D. Kohler, S. F. Wondimu, L. Hahn, I. Allegro, M. Blaicher, W. Freude, and C. Koos, "Lasing in Si3N4-organic hybrid (SiNOH) spiral resonators, " in *CLEO Conference 2018*, paper SM4I.6.

26. D. Kohler, I. Allegro, S. F. Wondimu, L. Hahn, W. Freude, and C. Koos, "Lasing in Si3N4-organic hybrid (SiNOH) waveguides," arXiv:1909.00020 [physics.optics], (2019).

27. F. Vogelbacher, J. Schotter, M. Sagmeister, J. Kraft, X. Zhou, J. Huang, M. Li, K.-J. Jiang, Y. Song, K. Unterrainer, and R. Hainberger, "Integrated silicon nitride organic hybrid DFB laser with inkjet printed gain medium," Opt. Express **27**(20), 29350–29356 (2019).

28. F. Vogelbacher, M. Sagmeister, J. Kraft, X. Zhou, J. Huang, M. Li, K.-J. Jiang, Y. Song, K. Unterrainer, and R. Hainberger, "Slot-waveguide silicon nitride organic hybrid distributed feedback laser," Sci. Rep. **9**(1), 18438 (2019).

29. D. Korn, M. Lauermann, S. Koeber, P. Appel, L. Alloatti, R. Palmer, P. Dumon, W. Freude, J. Leuthold, and C. Koos, "Lasing in silicon–organic hybrid waveguides," Nat. Commun. **7**(1), 10864 (2016).

30. A. Yariv, "Critical coupling and its control in optical waveguide-ring resonator systems," IEEE Photonics Technol. Lett. **14**(4), 483–485 (2002).

31. H. Kogelnik and C. V. Shank, "Coupled-wave theory of distributed feedback lasers," J. Appl. Phys. **43**(5), 2327–2335 (1972).

32. C. V. Shank, "Physics of dye lasers," Rev. Mod. Phys. **47**(3), 649–657 (1975).

33. V. M. Bondar, O. V. Przhonska, and Y. A. Tikhonov, "Inhomogeneous broadening of organic dyes in polymeric media: Nonlinear transmission spectra and photochemical kinetics," J. Phys. Chem. **96**(26), 10831–10837 (1992).

34. G. Grau and W. Freude, *Optische Nachrichtentechnik. Eine Einführung (Introduction to Optical communications)* (Springer, 2005).

35. T. Grossmann, *Whispering-Gallery-Mode Lasing in Polymeric Microcavities* (dissertation, Karlsruhe Institute of Technology, 2012).

36. Md. M. Mazumder, G. Chen, and R. K. Chang, "Wavelength shifts of dye lasing in microdroplets: effect of absorption change," Opt. Lett. **20**(8), 878–880 (1995).

37. S. Krämmer, S. Rastjoo, T. Siegele, S. F. Wondimu, C. Klusmann, C. Koos, and H. Kalt, "Size-optimized polymeric whispering gallery mode lasers with enhanced sensing performance," Opt. Express **25**(7), 7884–7894 (2017).

38. S. Chenais and S. Forget, "Recent advances in Solid-State Organic Lasers," Polym. Int. **61**(3), 390–406 (2012).

39. M. Lehnhardt, T. Riedl, T. Weimann, and W. Kowalsky, "Impact of triplet absorption and triplet-singlet annihilation on the dynamics of optically pumped organic solid-state lasers," Phys. Rev. B **81**(16), 165206 (2010).

40. M. A. Ali, J. Moghaddasi, and S. A. Ahmed, "Examination of temperature effects on the lasing characteristics of rhodamine cw dye lasers," Appl. Opt. **29**(27), 3945–3949 (1990).

41. T. Susdorf, D. del Aqua, A. Tyagi, A. Penzkofer, O. García, R. Sastere, A. Costela, and I. García-Moreno, "Photophysical characterization of pyrromethene 597 laser dye in silicon-containing organic matrices," Appl. Phys. B **86**(3), 537–545 (2007).

42. S. Forget and S. Chénais, *Organic solid-state lasers* (Springer, 2013).

43. A. Diaspro, G. Chirico, C. Usai, P. Ramoino, and J. Dobrucki, *Handbook of biological confocal microscopy, Photobleaching* (Springer, 2006), Chap. 39.

44. G. Gupta and W. H. Steier, "Modeling Photobleaching of Optical Chromophores: Light-Intensity Effects in Precise Trimming of Integrated Polymer Devices," J. Phys. Chem. C **112**(21), 8051–8060 (2008).